Available online at www.sciencedirect.com

ScienceDirect

Procedia Engineering 79 (2014) 17 – 27

Procedia Engineering

www.elsevier.com/locate/procedia

37th National Conference on Theoretical and Applied Mechanics (37th NCTAM 2013) & The 1st International Conference on Mechanics (1st ICM)

A comparison of coarse-resolution numerical simulation with experimental measurements of wind turbine aerodynamic performance

Ping Ma[a], Meishen Li[a], Jonathan Jilesen[b], Fue-Sang Lien[a*], Eugene Yee[c], Howard Harrison[b]

[a]*Department of Mechanical and Mechatronics Engineering, University of Waterloo, Waterloo, Ontario, N2L 3G1, Canada*
[b] *GTRenergy Ltd., Oakville, Ontario, L6H 5V1, Canada*
[c]*Defence R&D Canada, Suffield, P.O. Box 4000, Stn Main, Medicine Hat, AB, T1A 8K6, Canada*

Abstract

Coarse-resolution computational fluid dynamics simulations using the unsteady Delayed-Detached-Eddy simulation (DDES) and the steady Reynolds-Averaged Navier-Stokes (RANS) methodologies were conducted to predict the aerodynamic performance of the Fortis Montana 5.8-kW horizontal-axis wind turbine (HAWT). The turbulence models used for the closure of the DDES and RANS methodologies were the one-equation Spalart-Allmaras model and the two-equation shear stress transport $k-\omega$ model, respectively. To assess and validate the predictive performance of these two simulation strategies conducted with coarse-resolution computational grids, experimental measurements of the Fortis Montana 5.8-kW HAWT were conducted at the 9 m $\times$ 9 m National Research Council Canada wind tunnel. Results of a detailed comparison between the wind tunnel experimental measurements and the model predictions are presented. It was found that predictions of the power curve using the DDES methodology yielded good conformance with the associated experimental measurements. Furthermore, it was found that the RANS method fails to capture the correct power output at moderate and high tip speed ratios. It is concluded that accuracy in a wind turbine power curve prediction using the relatively coarse mesh in this study is probably satisfactory for most real-world industrial and engineering applications.

Selection and peer-review under responsibility of the National Tsing Hua University, Department of Power Mechanical Engineering

Keywords: wind turbine; power curve; power coefficient; RANS; DDES; HAWT

* Corresponding author. Tel.: +1-519-888-4567 ext 36528 ; fax:+1-519-885-5862
E-mail address: fslien@uwaterloo.ca

Selection and peer-review under responsibility of the National Tsing Hua University, Department of Power Mechanical Engineering
doi:10.1016/j.proeng.2014.06.304

1. Introduction

The utilization of wind energy is experiencing phenomenal worldwide growth driven by declining costs of wind power generation, growing electricity demand from clean energy sources and mounting environmental concerns, particularly over climate change [1]. Prediction of the aerodynamic loads on a horizontal-axis wind turbine (HAWT) is an important process because it is directly related to crucial characteristics of the wind turbine, such as its power curve, structural loads, and noise generation. As wind turbines increase in size and power output, measurements of wind turbine aerodynamics have become increasingly more difficult and too expensive to undertake. As a consequence, numerical methods have been used more and more to analyze the wind turbine aerodynamics during the design stage. However, owing to various difficulties arising from the three-dimensionality, unsteadiness and dynamic flow separations in the problem, the development of an accurate, reliable and robust numerical prediction tool for wind turbine aerodynamic loads remains a significant challenge for the wind energy industry.

The wind turbine power curve is a critical characteristic that needs to be predicted accurately for the evaluation of its potential power generation. Towards this purpose, early attempts have focused on application of the blade element momentum (BEM) [2-3] and the vortex lattice (VL) [4] methods for wind turbine power prediction. However, the inboard stall and stall delay models used in these methods have been shown to exhibit various discrepancies in their predictions of the rotor power at higher wind speeds. Furthermore, these methods assume implicitly that adequate airfoil tables [5] are available for the various wind turbine designs which prohibits their general application in wind turbine power prediction. With increasing computational power, methodologies for wind turbine power prediction based on computational fluid dynamics (CFD) such as Reynolds-averaged Navier-Stokes (RANS) approaches have been applied. Sankar and co-workers [6-8] developed a hybrid Navier-Stokes (N-S)/Full-Potential/Free Wake method for predicting three-dimensional viscous flows over a HAWT and achieved an overall good agreement with some experimental data. Even so, the predicted wind turbine power here was seen to exhibit various discrepancies when compared with available experimental measurements. Various investigators [9-12] have applied RANS with the $k-\omega$ or SST $k-\omega$ turbulence model (implemented using in-house codes) to simulate the complex flow field around the National Renewable Energy Laboratory (NREL) phase VI wind turbine. In these investigations, the predictions for the power generated by the wind turbine were in good agreement with the experimental data for the attached and moderately stalled flow conditions, but discrepancies in the predictions were observed for the stalled flow regime. Sagol et al. [13] tested the predictive accuracy of different turbulence models within the RANS framework for wind turbine power generation using the commercial software ANSYS Fluent. Among the turbulence models used in their paper (the standard $k-\varepsilon$, the RNG $k-\varepsilon$, the realizable $k-\varepsilon$ and the SST $k-\omega$ turbulence models), they concluded that the SST $k-\omega$ model was the most appropriate turbulence model for wind turbine flow simulations. They compared their predictions with some experimental data and showed that the predicted wind turbine power from these models underestimated the corresponding experimental measurements for all wind speeds tested. The reasons for this discrepancy were attributed to the poor performance of the RANS models when applied to the highly separated flows and to the use of a relatively coarse mesh around the leading-edge region of the rotor blades.

This paper focuses on using the commercial software ANSYS Fluent for the prediction of the wind turbine power output. This objective of the research here is on providing more accurate predictions of the wind turbine power output with CFD using less computational resources than those required in previous investigations [6-13] (which involved both in-house codes and commercial software for CFD). To this purpose, the simulation of the highly-disturbed and complex flow field about a newly-designed HAWT at different tip speed ratios (TSRs) is performed and these predictions are compared with some new experimental data obtained in the wind tunnel facility at National Research Council Canada. The research reported herein used both the DDES and RANS methodologies on a relatively coarse mesh (mimicking the computational limits available for common engineering applications) and compared their predictions of the wind turbine power curve with our new experimental measurements. SHARCNET (www.sharcnet.ca), which is a consortium of Canadian academic institutions who share a network of high performance computers, provided the computing resources for all the simulations conducted in this paper.

2. Experimental measurements

The Fortis Montana is a 5.8-kW permanent magnet wind turbine. Each blade of the wind turbine has a diameter of 5.03 m and a swept area of 19.87 m^2. The approximate exposed area of the hub and mast was 0.18 m^2 during the experimental testing. The blade cord at 75% of the blade length was 0.2135 m.

The experimental testing of the Fortis Montana 5.8-kW wind turbine was conducted at the 9 m × 9 m National Research Council Canada wind tunnel. The nacelle of the wind turbine was mounted without any tilt at the center of the wind tunnel on a custom stand. The mast of the stand was 4.55 m in length and extended 4.16 m above the wind tunnel floor. A cardboard fairing, measuring 0.28 m in diameter shrouded the mast in order to shield it from aerodynamic loads. The fairing was mounted to the tunnel floor independent of the tunnel mass balance and had an approximate frontal area of 1.16 m^2. A sensor was installed on the mast to detect if there was any fowling between the mast and shroud. Contaminated results were removed from the results presented in this study.

Preliminary testing was conducted without the blades to determine the shield and mast/generator/hub blockage components. The correction used to estimate these quantities was the Maskell III correction [14], while the rotor blockage was calculated based on a momentum correction described by Glauert [15]. Using these corrections, the performance within the tunnel was projected to that of a representative free stream wind speed.

The forces acting on the wind turbine were measured using a mass balance methodology. This mass balance was located below the floor of the tunnel. Testing on the wind turbine was conducted at wind speeds of 6, 7, 8, 9 and 10 m s^{-1} in order to determine when Reynolds number independence had been reached. The testing was conducted under smooth flow conditions with the free stream turbulence intensity of about 0.75%. During testing, the drift in the mass balance was closely monitored in order to keep the uncertainty of the power coefficient, C_p, to less than 1%. The turbine tip speed was controlled by varying the load on the turbine generator using two Chroma 63204 DC electronic loads. The wind turbine speed was measured using a remote optical sensor (ROS-W Monarch Instruments) by affixing reflective tape near the hub of each turbine blade.

It was found that the power coefficient versus TSR curves for wind speeds of 7 m s^{-1} and above converged, showing Reynolds number independence, so it is these results which were used for generating the TSR curve used for our model comparisons below.

3. Theoretical framework

Two different computational methodologies were used to predict the wind turbine power curve; namely, a hybrid large-eddy simulation (LES) and RANS approach and a conventional RANS approach using the shear-stress transport (SST) $k-\omega$ model for turbulence closure. The turbulence closure models used in these two computational methodologies were originally designed as low-Re-number models. However, owing to the coarse mesh that was used in the current simulations, wall functions were applied instead by ANSYS Fluent, whenever the centroid of the wall adjacent cell lay within the log-law region of the boundary layer [16]. Within this log-law region,

$$\frac{u}{u_\tau}=\frac{1}{\kappa}\ln E\left(\frac{\rho u_\tau y}{\mu}\right), \tag{1}$$

where u is the velocity parallel to the wall, u_τ is the friction velocity, y is the normal distance from the wall, and the model constants have the following values: $\kappa=0.41$ [see also Eqs. (3) and (11)] and $E=9.793$.

3.1. DDES model with the Spalart-Allmaras (S-A) turbulence closure

The hybrid RANS/LES methodology combines the computational efficiency of RANS for modeling the flow in the near-wall regions of a solid surface with the predictive accuracy of LES for simulating the large-scale turbulent flow structures in regions away from a solid surface. The particular form of hybrid RANS/LES used in this paper is

DDES, which utilizes an unsteady RANS model near the solid surface within the wall boundary layer and transitions smoothly to LES away from the wall by introducing a characteristic length scale $\tilde{d}$ defined by

$$\tilde{d} = d - f_d \max(0, d - \mathrm{C_{DES}}\,\Delta), \tag{2}$$

where d is the distance to the wall, Δ is the maximum computational cell dimension in the *x*-, *y*- and *z*-directions. The empirical constant $\mathrm{C_{DES}}$ in Eq. (2) has a value of 0.65. As an improved version of DES, DDES ensures that the transition from RANS to LES is independent of grid spacing by introducing a blending function f_d given by Eq. (3), which is similar to the one used by Menter and Kuntz [17] for the SST $k-\omega$ turbulence model [18]; namely,

$$f_d = 1 - \tanh\left[\left(8r_d\right)^3\right],\ r_d = \frac{\nu_t + \nu}{\left(\frac{\partial u_i}{\partial x_j}\frac{\partial u_i}{\partial x_j}\right)^{1/2}\kappa^2 d^2}, \tag{3}$$

where ν and ν_t are the molecular and turbulent kinematic viscosities, respectively.

In the case of the S-A turbulence model [19], only one additional transport equation is solved. This transport equation is for the modified turbulent kinematic viscosity $\tilde{\nu}$, which is identical to the turbulent kinematic viscosity except in the near-wall region; namely,

$$\frac{\partial}{\partial t}\left(\rho\tilde{\nu}\right) + \frac{\partial}{\partial x_j}\left(\rho\tilde{\nu}u_j\right) = \frac{\partial}{\partial x_j}\left[\left(\frac{\mu + \rho\tilde{\nu}}{\sigma_{\tilde{\nu}}}\right)\frac{\partial\tilde{\nu}}{\partial x_j}\right] + C_{b2}\rho\left(\frac{\partial\tilde{\nu}}{\partial x_j}\right)^2 + G_\nu - Y_\nu. \tag{4}$$

The turbulent viscosity production G_ν, and turbulent viscosity destruction Y_ν, are determined from the following parameterization:

$$G_\nu = C_{b1}\rho\tilde{\Omega}\tilde{\nu},\ Y_\nu = C_{w1}\rho f_w\left(\tilde{\nu}/\tilde{d}\right)^2, \tag{5}$$

where

$$\begin{aligned}
&\tilde{\Omega} = \Omega + \frac{\tilde{\nu}}{\kappa^2\tilde{d}^2}f_{\nu 2},\ f_{\nu 2} = 1 - \frac{\chi}{1+\chi f_{\nu 1}},\ f_{\nu 1} = \frac{\chi^3}{\chi^3 + C_{\nu 1}^3},\ \chi = \tilde{\nu}/\nu,\ f_w = g\left(\frac{1+C_{w3}^6}{g^6 + C_{w3}^6}\right)^{1/6},\\
&g = r + C_{w2}(r^6 - r),\ r = \frac{\tilde{\nu}}{\tilde{\Omega}\kappa^2\tilde{d}^2},\ \Omega = \sqrt{2\Omega_{ij}\Omega_{ij}},\ \Omega_{ij} = \frac{1}{2}\left(\frac{\partial u_i}{\partial x_j} - \frac{\partial u_j}{\partial x_i}\right).
\end{aligned} \tag{6}$$

The closure constants used in the S-A model are specified as follows:

$$\begin{aligned}
&C_{b1} = 0.1355,\ C_{w1} = \frac{C_{b1}}{\kappa^2} + \frac{\left(1 + C_{b2}\right)}{\sigma_{\tilde{\nu}}},\ C_{b2} = 0.622,\\
&\sigma_{\tilde{\nu}} = 2/3,\ C_{\nu 1} = 7.1,\ C_{w2} = 0.3,\ C_{w3} = 2.0.
\end{aligned} \tag{7}$$

The turbulent dynamic viscosity is then calculated using $\mu_t = \rho\tilde{\nu}f_{\nu 1}$.

3.2. RANS model with the SST $k-\omega$ turbulence closure

Two additional transport equations are solved in the SST $k-\omega$ turbulence model [20], where k is the turbulence kinetic energy and ω is the dissipation per unit turbulence kinetic energy:

$$\frac{\partial}{\partial t}(\rho k)+\frac{\partial}{\partial x_j}(\rho k u_j)=\frac{\partial}{\partial x_j}\left[\left(\mu+\frac{\mu_t}{\sigma_k}\right)\frac{\partial k}{\partial x_j}\right]+\tilde{G}_k-Y_k, \tag{8}$$

$$\frac{\partial}{\partial t}(\rho \omega)+\frac{\partial}{\partial x_j}(\rho \omega u_j)=\frac{\partial}{\partial x_j}\left[\left(\mu+\frac{\mu_t}{\sigma_\omega}\right)\frac{\partial \omega}{\partial x_j}\right]+G_\omega-Y_\omega+D_\omega. \tag{9}$$

The generation of k and ω, $\tilde{G}_k$ and G_ω, the cross diffusion term D_ω, and σ_k and σ_ω are calculated by the following equations:

$$\begin{aligned}&\tilde{G}_k=\min(G_k,10\rho\beta^* k\omega),\ G_\omega=\frac{\alpha}{\nu_t}\tilde{G}_k,\ D_\omega=2(1-F_1)\rho\sigma_{\omega,2}\frac{1}{\omega}\frac{\partial k}{\partial x_j}\frac{\partial \omega}{\partial x_j},\\&\sigma_k=\left[(F_1/\sigma_{k,1})+((1-F_1)/\sigma_{k,2})\right]^{-1},\ \sigma_\omega=\left[(F_1/\sigma_{\omega,1})+((1-F_1)/\sigma_{\omega,2})\right]^{-1},\end{aligned} \tag{10}$$

where

$$\begin{aligned}&G_k=-\rho\overline{u_i'u_j'}\frac{\partial u_j}{\partial x_i},\ \alpha=\frac{\alpha_\infty}{\alpha^*}\left(\frac{\alpha_0+\mathrm{Re}_t/R_\omega}{1+\mathrm{Re}_t/R_\omega}\right),\ \alpha^*=\alpha_\infty^*\left(\frac{\alpha_0^*+\mathrm{Re}_t/R_k}{1+\mathrm{Re}_t/R_k}\right),\ \alpha_\infty=F_1\alpha_{\infty,1}+(1-F_1)\alpha_{\infty,2},\\&F_1=\tanh(\Phi_1^4),\ \Phi_1=\min\left[\max\left(\frac{k^{1/2}}{\beta^*\omega y},\frac{500\mu}{\rho y^2\omega}\right),\frac{4\rho k}{\sigma_{\omega,2}D_\omega^+ y^2}\right],\ \alpha_{\infty,1}=\beta_{i,1}/\beta_\infty^*-\kappa^2(\sigma_{\omega,1})^{-1}(\beta_\infty^*)^{-1/2},\\&\alpha_{\infty,2}=\beta_{i,2}/\beta_\infty^*-\kappa^2(\sigma_{\omega,2})^{-1}(\beta_\infty^*)^{-1/2},\ \mathrm{Re}_t=\frac{\rho k}{\mu\omega},D_\omega^+=\max\left(2\rho\frac{1}{\sigma_{\omega,2}}\frac{1}{\omega}\frac{\partial k}{\partial x_j}\frac{\partial \omega}{\partial x_j},10^{-10}\right).\end{aligned} \tag{11}$$

In Eq. (11), $-\rho\overline{u_i'u_j'}$ is the Reynolds stress tensor which is modeled using the Boussinesq assumption. The dissipation of k and ω, Y_k and Y_ω, are determined using the following equations:

$$Y_k=\rho\beta_i^* k\omega,\ Y_\omega=\rho\beta_i\omega^2,\ \beta_i^*=\beta_\infty^*\left[\frac{4/15+(\mathrm{Re}_t/R_\beta)^4}{1+(\mathrm{Re}_t/R_\beta)^4}\right],\ \beta_i=F_1\beta_{i,1}+(1-F_1)\beta_{i,2}. \tag{12}$$

Finally, the turbulent viscosity is computed using the following equation:

$$\mu_t=\frac{\rho k/\omega}{\max\left(\frac{1}{\alpha^*},\frac{SF_2}{a_1\omega}\right)},\ S=\sqrt{2S_{ij}S_{ij}},\ S_{ij}=\frac{1}{2}\left(\frac{\partial u_i}{\partial x_j}+\frac{\partial u_j}{\partial x_i}\right),\ F_2=\tanh(\Phi_2^2),\ \Phi_2=\max\left(\frac{2k^{1/2}}{\beta^*\omega y},\frac{500\mu}{\rho y^2\omega}\right). \tag{13}$$

The closure constants used in the SST $k-\omega$ model take the following values:

$$\alpha_\infty^* = 1,\ \alpha_0 = 1/9,\ \alpha_0^* = \beta_i/3,\ \beta_\infty^* = 0.09,\ \beta_i = 0.072,\ a_1 = 0.31,\ \sigma_{k,1} = 1.176,\ \sigma_{k,2} = 1.0,$$
$$\sigma_{\omega,1} = 2.0,\ \sigma_{\omega,2} = 1.168,\ \beta^* = 0.09,\ \beta_{i,1} = 0.075,\ \beta_{i,2} = 0.0828,\ R_\beta = 8,\ R_k = 6,\ R_\omega = 2.95. \quad (14)$$

4. Numerical framework

The computational domain for the problem consists of two sub-domains: (a) the cylindrical rotating sub-domain surrounding the rotor and (b) the rectangular stationary sub-domain representing the external flow as shown in Fig. 1. The length of the computational domain extends from 1*D* (*D* is the rotor diameter) upwind to 3*D* downwind of the wind turbine.

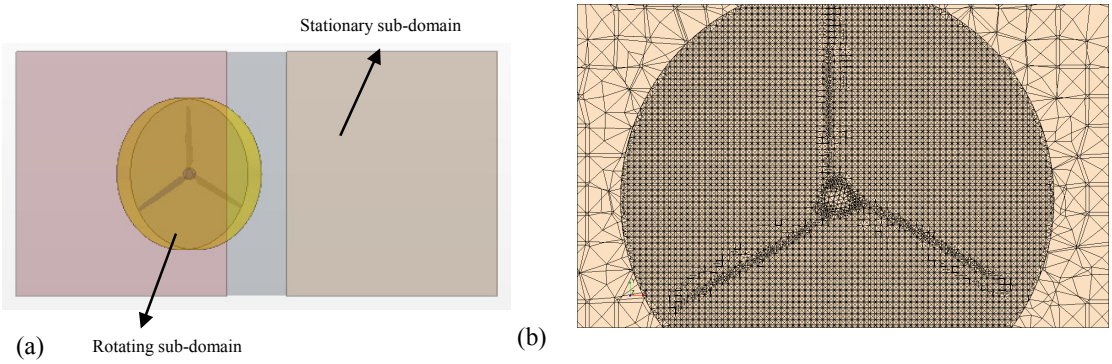

Fig. 1. (a) Geometry of the computational domain; (b) tetrahedral mesh used for the discretization of the rotating and stationary sub-domains.

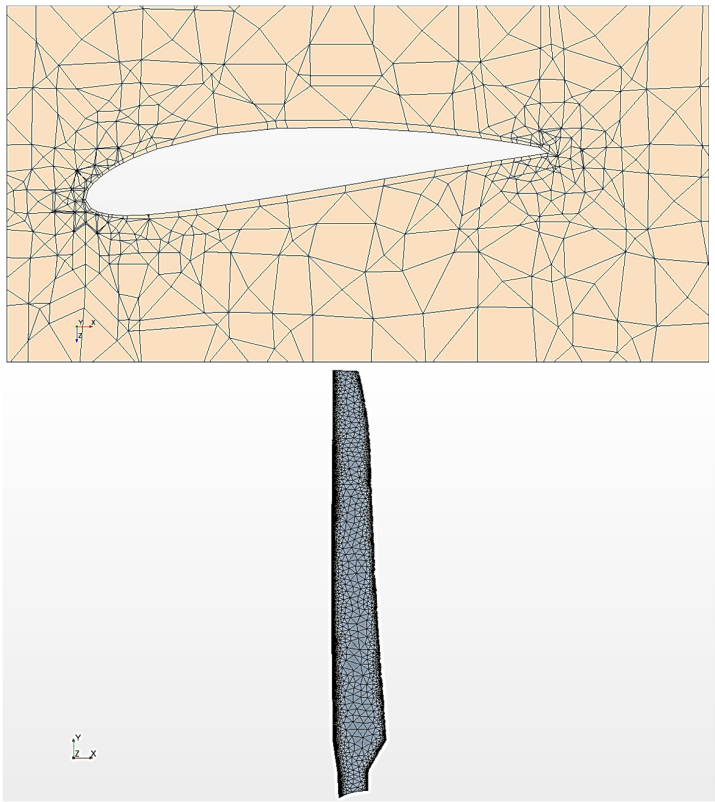

Fig. 2. Fine tetrahedral mesh used for the discretization of the three blades comprising the turbine rotor.

An unstructured grid consisting of 1.31 million tetrahedral cells clustered around the rotor and hub in the rotating sub-domain, with a total of 1.48 million tetrahedral cells for whole computational domain (comprising the rotating and stationary sub-domains) was created with the ANSYS design modeler. The computational grid is shown in Fig. 2. One layer of prismatic cells was generated surrounding the blade having cell centroids with normalized wall-normal distances y^+ in the range of 30 to 200 as shown in Fig. 2(a). Fig. 2(b) displays the computational mesh used to represent the blade. A higher-resolution grid was generated surrounding the turbine blade in the vicinity of both the leading and trailing edges of the blade. Due to the limitation of ANSYS Fluent licenses available on SharcNet, the computational grid shown here for representation of the turbine rotors in the rotating sub-domain and the surrounding air flow of the wind tunnel in the stationary sub-domain constitutes a relatively coarse-grid representation for the problem.

The simulations of the flow field were undertaken using ANSYS Fluent 13.0. A pressure-based solver was used for the incompressible flow calculation. Both the RANS and DDES computational strategies were conducted. As mentioned earlier, the RANS calculations used the two-equation SST $k-\omega$ turbulence model, whereas the DDES calculations employed the one-equation S-A turbulence model.

The Multiple Rotating Reference Frame (MRF) method is used for both the RANS and DDES calculations. The MRF model is a steady-state approximation that allows the stationary and rotating sub-domains to be assigned different rotational and translational velocities. The wind turbine rotor is in the rotating domain, whereas the wind tunnel is in the stationary domain. For our current application, the interaction of the flow at the interface between the rotating and stationary sub-domains is relatively weak and uncomplicated, implying that MRF can be used to a very good approximation if our main interest is to predict the power output from the wind turbine rotor (for, otherwise, the more complicated but more exact sliding mesh methodology must be utilized). In the RANS calculations, the disturbed flow in both the rotating and stationary sub-domains is treated as being statistically stationary, whereas in the DDES calculations the flow in both sub-domains is treated as being transient.

The three-dimensional steady (for RANS) and unsteady (for DDES) Navier-Stokes equations were solved using a cell-centered finite volume method. A least-squares cell-based scheme was chosen for the gradient approximation of all quantities used in the discretization of the governing equations. A first-order upwind scheme was used to approximate the convective terms in the transport equations for the turbulence kinetic energy and viscous dissipation rate in the SST $k-\omega$ model and in the modified turbulence viscosity transport equation in the S-A model. A pressure-weighted interpolation scheme was used to estimate the pressure values at the cell faces from their values at the cell centroids. For the momentum equation, a bounded central differencing scheme was used in DDES and a second-order upwind scheme was employed in RANS for discretization of the convective term in the momentum transport equation. All the diffusion terms in the various transport equations were discretized using a central differencing scheme. A second-order implicit scheme was chosen for the time marching algorithm with a fixed time step of 0.0001s to keep the average Courant-Friedrichs-Lewy (CFL) number within the computational domain below a value of 2. In the solution of the discretized equations, a maximum of 50 iterations was permitted for each time step. The iterative scheme used here to enforce mass conservation through the pressure-velocity coupling was the Semi-Implicit Method for Pressure-Linked Equations (SIMPLE).

A uniform (nominal) mean velocity of 7 m s^{-1} was prescribed at the inlet of the computational domain (for the RANS simulations and one set of DDES simulations as described in detail later). For the specification of the turbulence at the inlet boundary, the turbulence intensity and the dissipation length scale for turbulence were prescribed according to the experimental data and the mixing-length assumption, and used for both the DDES and RANS calculations. The pressure at the outlet boundaries of the domain was set to atmospheric pressure. The wind turbine blade surfaces were treated as no-slip smooth walls. Owing to the fact that the absolute velocity formulation is used in all our simulations, no special transformation is required at the interface between the two sub-domains. Scalar quantities, such as pressure, are determined locally from the adjacent cells.

5. Results and discussion

Figure 3 exhibits the predicted torque histories for the wind turbine using DDES and RANS methods for TSR $\lambda = 5.21$, where $\lambda = 2\pi Rf/U$, R is the radius of the turbine blades, f is the angular velocity of the blades (rev s^{-1}), and U is the approach wind speed (m s^{-1}). For the transient DDES simulation, it can be seen that the torque time history was stabilized after roughly 10,000 time steps. In contrast, in the steady RANS simulation, the torque converged to a constant value after only about 350 iterations. We note that the convergence histories of the torque are similar to those shown in Fig. 3 for the other TSR values (not shown). The CPU time for a RANS calculation is less than 1 hour, while a DDES calculation requires approximately 40 hours of CPU time on SharcNet. Owing to the fact that the DDES simulation resolves some of the relevant scales in the turbulence and hence captures the flow field unsteadiness, it is expected that the time series for the torque for this case would take longer to stabilize to a quasi-steady value than that for the steady RANS simulation. In spite of this, the DDES method yielded generally more accurate predictions of the turbine power output and power coefficients than the RANS method.

Figure 3(c) exhibits the predicted power coefficient C_p obtained using the two simulation methodologies in comparison with that obtained from our wind tunnel measurements for various values of TSR. The DDES simulation labeled DDES_SA_1 and the RANS simulation in Fig. 3(c) utilize the same nominal inlet velocity of 7 m s^{-1} for each of the different TSRs considered in the experimental measurements. In contrast, the DDES simulation labeled DDES_SA_2 utilizes the exact inlet velocity that was used in the experiments; namely, inlet velocity values of 7 m s^{-1}, 8 m s^{-1}, 9 m s^{-1}, and 10 m s^{-1} respectively, at the four increasing values of TSR at which the power coefficient was measured.

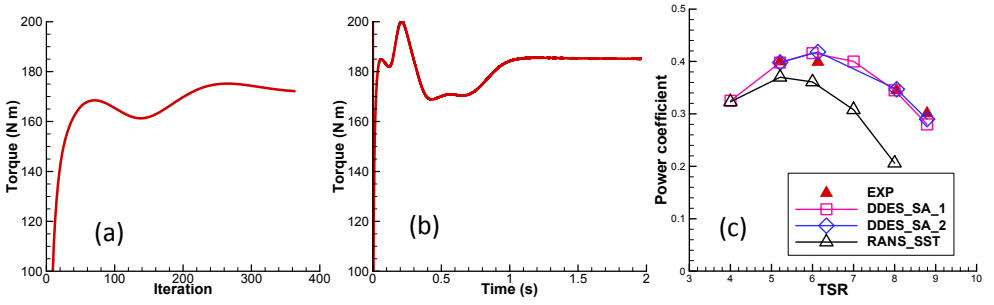

Fig. 3. Convergence histories for torque obtained using (a) RANS and (b) DDES calculations for λ=5.21. (c) Comparison of the measured C_p with the predicted C_p obtained using the DDES and RANS simulation methodologies.

It is noted that the RANS simulation generally under-predicts C_p at each of the TSRs for which measurements are available, and the degree of this under-prediction increases with increasing values of the TSR. This conforms to the results obtained by Sagol et al [13] who reported an under-prediction of C_p for a wind turbine using a RANS simulation approach. The predictions of C_p provided by the DDES simulation (whether DDES_SA_1 or DDES_SA_2) are superior to those provided by the RANS simulation. This is likely due to the fact that DDES resolves the large scale eddies away from the walls and this resolved flow information in turn improves the lift (and torque) prediction. Note that the DDES simulation slightly over-predicts C_p at $\lambda = 6$, whereas it slightly under-predicts C_p at $\lambda = 8.79$ as seen in Fig. 3(c). Although predictions of C_p provided by the RANS and DDES simulations agree at $\lambda = 4$, the predictions provided by these two methodologies increasingly diverge from each other at increasing values of the TSR.

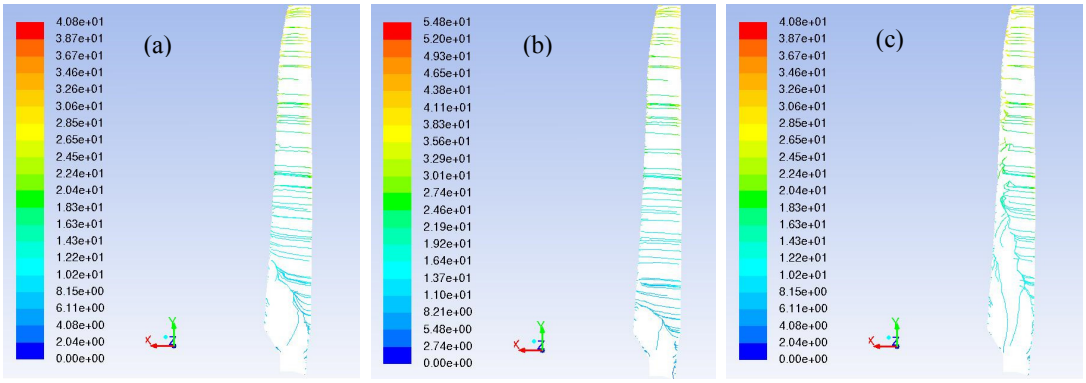

Fig. 4. Blade oil flow pathlines at the spanwise location y = 0.9R. (a) λ = 5.21, DDES_SA_1; (b) λ = 7, DDES_SA_1; (c) λ = 5.21, RANS.

Figure 4 displays blade oil flow pathlines at $y = 0.9R$ in the spanwise direction for different TSR values using the DDES_SA_1 and RANS methods. The color legend for the plots of the flow pathlines encodes the magnitude of the absolute velocity (in m s^{-1}). At $\lambda = 5.21$, the angle of attack (AOA) at blade root area is relatively high in comparison with the blade tip area. This results in the flow separation around the blade root area as shown in Fig. 4(a). As the TSR increases to a value of 7 [Fig. 4(b)], the AOA begins to decrease and the resulting aerodynamics is associated with a more pronounced attached flow field surrounding the blade, leading to a smaller separation zone in the root area of the blade. In this regime, the wind turbine achieves a higher power output as can be seen from Fig. 3(c). However, at still higher values of the TSR, say at $\lambda = 8.79$, the AOA decreases further and the lift generated by the blade decreases as a consequence, resulting in a reduced power output from the wind turbine as is evident from Fig. 3(c). Fig. 4(c) depicts the blade oil flow pathlines at $y = 0.9R$ in the spanwise direction at $\lambda = 5.21$ using the RANS method. Compared to the results of the DDES simulation shown in Fig. 4(a), it is seen that the RANS simulation predicts a larger separation zone at the blade root area. This separation zone extends up to two thirds of the blade length in the spanwise direction. In consequence, this result implies that the RANS simulation methodology has the tendency to overestimate the power losses from the flow field around the turbine in comparison to that given by the DDES simulation methodology. As a result of this tendency, a lower wind turbine torque as well as a correspondingly lower power coefficient is predicted using the RANS simulation methodology as compared to the DDES methodology. This is consistent with the results for predictions of the wind turbine power coefficients summarized in Fig. 3(c).

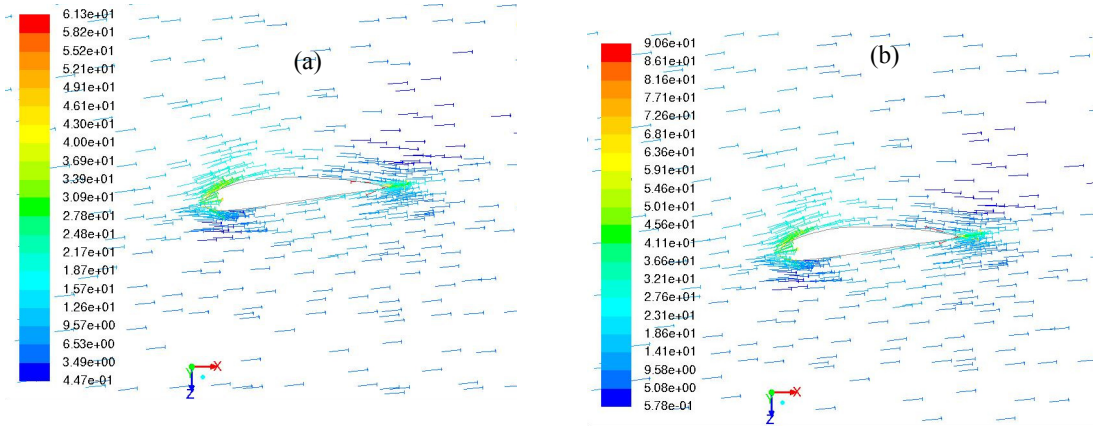

Fig. 5. Velocity vector plot at the spanwise location y = 0.9R at λ = 8.79. The unit of the velocity vector is in m s^{-1}**.** (a): DDES_SA_1; (b): DDES_SA_2.

From Fig. 3(c), it can be seen that the DDES_SA_2 simulation gives a predicted value of the power coefficient that agrees slightly better with the associated measured value than that given by the DDES_SA_1 simulation at $\lambda = 8.79$. The reason for this better agreement can be seen by an examination of Fig. 5. It is noted from the velocity vector plot that the DDES_SA_2 simulation (which uses the exact inlet velocity of 10 m s^{-1} as used in the experiment) results in a higher relative velocity magnitude on the suction side of the airfoil than the comparable simulation provided by DDES_SA_1 which uses a nominal inlet velocity of 7 m s^{-1}. Using the correct and larger value of the inlet velocity gave a prediction for the power coefficient that was in slightly better conformance with the associated measured value.

6. Conclusions

Although the DDES simulation methodology requires a more significant computational effort (about 40 times more CPU hours) than the RANS simulation methodology, it was found in the present study that the DDES results agree much better with the experimental measurements for the wind turbine power coefficient (a critical quantity for assessing aerodynamic performance) than the RANS results. This is because RANS calculation can only provide a time-averaged mean value for velocity field, whereas DDES method is capable of resolving the larger-scale turbulence structures and also taking into account the unsteadiness generated in the flow field. Furthermore, the discrepancy between the predictions of the power coefficient provided by the DDES simulation methodology and the experimental measurements is comparable to the errors in the measurements (i.e., within 1%), which is encouraging. In consequence, the results in this paper appear to indicate that a relatively coarse-resolution DDES simulation can be used to provide reliable estimates for the power coefficient of a wind turbine for engineering application.

Strictly speaking, the computational mesh used for the DDES simulations in this study is still too coarse to provide a true scale-resolving turbulent fluid flow simulation around the wind turbine. However, despite this limitation, the accuracy in characterization of the aerodynamic performance of a wind turbine using a coarse-resolution DDES simulation methodology appears to provide a sufficient accuracy and a relatively low computational burden that it can be used in routine industrial and engineering applications. In this respect, the use of a DDES simulation methodology for these types of applications is recommended over the use of the SST $k-\omega$ RANS simulation methodology. For future work, the use of a finer mesh together with the sliding mesh methodology and various unsteady RANS and DDES turbulence models will need to be investigated in order to support the conclusions drawn herein based on the present preliminary coarse-grid MRF calculations.

References

[1] Global Wind Energy Council, Global Wind Report Annual Market Update 2011, 2011.
[2] R. G. Rajagopalan, J. B. Fanucci, Finite difference model for the vertical axis wind turbines, J. Propul. Power 1 (1985) 432–436.
[3] C. Leclerc, C. Masson, Predictions of Aerodynamic Performance and Loads of HAWTS Operating in Unsteady Conditions, AIAA Paper 99-0066, 1999.
[4] J. Whale, C. J. Fisichella, M. S. Selig, Correcting Inflow Measurements from HAWTS using a Lifting Surface Code, AIAA Paper 99-0040, 1999.
[5] E. P. N. Duque, Wa. Johnson, C. P. VanDam, R. Cortes, K. Yee, Numerical Predictions of Wind Turbine Power and Aerodynamic Loads for the NREL Phase II Combined Experimental Rotor, AIAA Paper 2000-0038, 2000.
[6] G. Xu, L. N. Sankar, Computational study of horizontal axis wind turbines, J. Sol. Energ. - T. ASME 122 (2000) 35–39.
[7] S. Benjanirat, L. N. Sankar, G. Xu, Evaluation of Turbulence Models for the Prediction of Wind Turbine Aerodynamics, AIAA Paper 2003-0517, 2003.
[8] S. Benjanirat, L. N. Sankar, Recent improvements to a combined Navier-Stokes full potential methodology for modeling horizontal axis wind turbines, in Proceedings of 23rd ASME Wind Energy Symposium, the 42nd AIAA Aerospace Sciences Meeting, Nevada, 2004, pp. 378–385.
[9] N. N. Sørensen, J. A. Michelsen, S. Schreck, Navier-Stokes predictions of the NREL phase VI rotor in the NASA Ames 80 ft × 120 ft wind tunnel, Wind Energy 5 (2002) 151–169.
[10] A. Le Pape, J. Lecanu, 3D Navier-Stokes computations of a stall-regulated wind turbine, Wind Energy 7 (2004) 309–324.
[11] S. Gómez-Iradi, R. Steijl, G. N. Barakos, Development and validation of a CFD technique for the aerodynamic analysis of HAWT, J. Sol. Energ. - T. ASME 131 (2009) 1–13.
[12] Y. Li, K.J. Paik, T. Xing, P. M. Carrica, Dynamic overset CFD simulations of wind turbine aerodynamics, Renew. Energ. 37 (2012) 285–298.
[13] E. Sagol, M. Reggio, A. Ilinca, Assessment of two-equation turbulence models and validation of the performance characteristics of an experimental wind turbine by CFD, ISRN Mech. Eng. 2012 (2012) 1–10.

[14] J. E. Hackett, K. R. Cooper, Extensions to Maskell's theory for blockage effects on bluff bodies in a closed wind tunnel, Aeronaut. J. 105 (2001) 409–418.
[15] H. Glauert, The Elements of Airfoil and Airscrew Theory, 2nd ed., Cambridge University Press, Cambridge, 1948.
[16] ANSYS Inc., ANSYS FLUENT 13.0: Theory Guide, 2010.
[17] F. R. Menter, M. Kuntz, Adaptation of eddy-viscosity turbulence models to unsteady separated flow behind vehicles, in: R. McCallen, F. Browand, J. Ross (Eds.), The Aerodynamics of Heavy Vehicles: Trucks, Buses and Trains,. Springer, Berlin Heidelberg, New York, 2004, pp. 339–359.
[18] H.S. IM, G.C. Zha, Delayed Detached Eddy Simulation of a Stall Flow Over NACA0012 Airfoil Using High Order Schemes, AIAA Paper 2011-1297, 2011.
[19] P. Spalart and S. Allmaras, A One-Equation Turbulence Model for Aerodynamic Flows, AIAA Paper 92-0439, 1992.
[20] F. R. Menter, Two-equation eddy-viscosity turbulence models for engineering application, AIAA J. 32 (1994) 1598–1605.